LAWRENCE
LIVERMORE
NATIONAL
LABORATORY

LLNL-JRNL-774207

Modeling hot spot experiments on shocked octahydro-1,3,5,7-tetranitro-1,3,5,7-tetrazocine

H. K. Springer, W. P. Bassett, S. Bastea, S. Stekovic, C. M. Tarver

May 14, 2019

Propellants, Explosives, Pyrotechnics

Disclaimer

Modeling hot spot experiments on shocked octahydro-1,3,5,7-tetranitro-1,3,5,7-tetrazocine

H. Keo Springer[a], Will P. Bassett, Sorin Bastea, Svjetlana Stekovic, Craig M. Tarver

Abstract: For the first time, mesoscale simulations of shocked explosives are validated with hot spot temperature data. Following recent experiments, we simulate a 25 μm aluminum flyer impacting a powder bed of octahydro-1,3,5,7-tetranitro-1,3,5,7-tetrazocine (HMX) with an initial speed of 1.4 to 3.6 km s^{-1}. The powder bed has a density of 0.56 g cc^{-1}, or 29% crystal density, and an average grain size of 4 μm. Simulations are performed in the multi-physics code, ALE3D. We employ a comprehensive HMX material model that accounts for the chemistry, unreacted and product equation-of-states (EOSs), elastic-plastic response, as well as melting and melt viscosity. Simulations show compaction, reaction, and gas jetting during the initial stages of shock in the powder bed. Shock reflection at the glass window interface increases hot spot temperatures in HMX product gas in excess of 7000K at higher impact speeds which is readily observable using pyrometry techniques. We extract a temperature histogram from simulations at discrete times, using it to calculate an effective emission spectrum and effective temperature, T_{eff}, for comparison to data. Simple T- and T^4-based methods inadequately weight the higher temperature regions and result in a low T_{eff} that is in poor agreement with data. However, calculating T_{eff} based on Planck's Law with a gray body assumption demonstrates good agreement with hot spot temperature data. A modified Arrhenius model is fit to the normalized reaction rates predicted by mesoscale simulations and inferred temperatures range from 1544 K to 1779 K. The agreement with experimental results validates our mesoscale simulations as useful tools for elucidating the role of hot spot mechanisms in the shock initiation of heterogeneous explosives.

1. Introduction

It is well known that bulk heating alone is insufficient to account for observed impact sensitivity in heterogeneous explosives, and that shock initiation in these materials is controlled by localized hot spots that form and grow at defects, e.g., pores, cracks, etc [1–6]. Due to the scarcity of direct measurements probing these microscale mechanisms, numerical simulations provide insights on these phenomena. Numerical studies have investigated sensitivities to impact pressure, pore size, pore morphology, multiple pores and grains, anisotropic crystal plasticity, rate-dependent strength, melt viscosity, and chemical kinetics [7–18]. Only recently have experimental studies measured hot spot temperatures in shocked HMX [19–21]. Such data is critical for gaining insights on heterogeneous initiation behavior and validating mesoscale modeling. In this study, we simulate recent hot spot experiments and compare results with published pyrometry-based temperature measurements [19].

2. Model Description

We perform mesoscale simulations using our multi-physics arbitrary Lagrangian Eulerian finite element hydrocode in 3D, ALE3D [22]. Our simulations consist of a 25 μm aluminum flyer impacting a 40 μm thick x 100 μm tall HMX powder bed sample backed by a glass window. The HMX powder bed density and grain size is 29% crystal density with a grain size of 4 μm. Computer generated microstructures are used to initialize the HMX powder bed in the sample region of simulation. Prescribed initial velocities of 1.4, 2.8, or 3.6 km s^{-1} are assigned to the aluminum flyer which impacts the sample. The numerical zone size in this study is 25 nm. Thermal diffusion is not activated in these simulations. While it is not entirely negligible, we do not believe that adding thermal diffusion would significantly change the conclusions drawn in the simulated time-frame of our study (10's nanoseconds).

2.1 HMX Material Model

Our comprehensive HMX material model accounts for the chemistry, unreacted and product equation-of-states (EOSs), elastic-plastic response, as well as melting and melt viscosity [18].

2.1.1 Strength and Melting

We employ an isotropic strength model that accounts for experimentally-observed dependencies on strain, strain rate, and temperature [23]. We believe this computationally efficient isotropic model is suitable for approximating the strength of a dilute HMX powder bed with numerous, randomly oriented grains. The yield strength is given by,

$$Y = (A + B\varepsilon^N)\left(1 + C\ ln(1 + \dot{\varepsilon}/\dot{\varepsilon}_0)\right)(1 - ((T - T_r)/\ (T_{melt} - T_r))^M) \quad (1)$$

where ε and $\dot{\varepsilon}$ are the equivalent plastic strain and strain rate, T is the temperature, T_r is room temperature, T_{melt} is the compression-dependent melt temperature. The quantities A, B, C, N, M and $\dot{\varepsilon}_0$ are material dependent constants; the model is informed by data across a range of strain rates [18]. We also use a high pressure, shear modulus, μ_0 [9]. The Lindemann Law describes HMX melting,

$$T_{melt} = T_{melt,0}\left(e^{(2a(1-v))}\right)\left((1/v)^{2(\gamma_0 - a - 1/3)}\right) \quad (2)$$

where v is the relative volume, $T_{melt,0}$ is the melt temperature at ambient pressure, γ_0 is Gruneisen gamma, and a is a correction to Gruneisen gamma [9]. Upon melting, the strength is set to zero and a constant melt viscosity is activated in the HMX until reaction occurs [14, 18]. Strength, melt, and viscosity model parameter values are given in Table 1.

A first order rate law captures the reaction evolution in the HMX where the rate coefficient, k, is given by an Arrhenius model fit to ignition time data across a wide range of temperatures [24],

$$d[HMX]/dt = -d[product\ gas]/dt = -k[HMX] \quad (3)$$

$$k = A_k e^{(-E_a/RT)} \quad (4)$$

Kinetic model parameters are also given in Table 1. The Arrhenius prefactor is increased such that $\ln(A_k)$ = 30.45 s^{-1} to better match pyrometry data which is appropriate given the uncertainties in extrapolating low pressure chemistry to the high pressure regime.

We employ the thermochemical code, Cheetah [25], for the HMX unreacted solid and product gas EOSs in our ALE3D simulations. A previous study [18] shows that the HMX unreacted EOS in Cheetah compares well with isothermal data [26, 27] and Hugoniot data [28, 29]. Also, the Cheetah EOS for CHNO reaction products mixtures is well tested for a wide range of materials and thermodynamic conditions [25, 30].

Table 1. HMX Material Model Parameters.

Parameter	Value	Units
A	100	MPa
B	100	MPa
C	1.14	None
N	0.1	None
M	3	None
$\dot{\varepsilon}_0$	10^{-3}	μs^{-1}
T_r	298	K
μ_0	11	GPa
$T_{melt,0}$	552	K
γ_0	1.1	None
a	1.53	None
η_0	55x10^{-2}	Poise
lnA_k	30.45	$\ln(s^{-1})$
E_a	35.6	kcal/mol

2.1.2 Aluminum Material Model

For the pure aluminum (Aluminum 1100) flyer, we employ a Johnson-Cook strength model and a Mie-Gruneisen EOS model where the pressure is given by,

$$P = \frac{\rho_0 c^2 \mu \left[1+(1-\gamma_0/2)\mu - b\mu^2/2\right]}{\left[1-(S_1-1)\mu\right]} + (\gamma_0 + b\mu)e \quad (5)$$

where $\mu = \rho/\rho_0 - 1$, ρ_0 and ρ are the initial and current densities, C and S_1 are the intercept and the slope of the U_s-U_p curve, γ_0 is the Gruneisen gamma, and e is the internal energy per unit volume. Model parameter values are given in Table 2.

Table 2. Aluminum 1100 Material Model Parameters.

Parameter	Value	Units
A	115	MPa
B	68	MPa
C	0.016	None
N	0.58	None
M	1.13	None
$\dot{\varepsilon}_0$	10^{-6}	μs^{-1}
T_r	294	K
$T_{melt,0}$	923	K
μ_0	27.1	GPa
ρ_0	2.707	g cm^{-3}
c	5.386	$km\ s^{-1}$
S_1	1.339	None
γ_0	1.97	None
b	0.48	None

2.1.3 Glass Material Model

We use a simple elastic-plastic model with yield strength, Y, and shear modulus, μ_0, as well as a Mie-Gruneisen EOS for the borosilicate glass window. The EOS is based on Hugoniot data in the applicable bulk shock pressure range [28]. This approach for modeling the glass window during early time compression is based on [31]. Model parameter values are given in Table 3.

Table 3. Glass Material Model Parameters.

Parameter	Value	Units
Y	5	GPa
μ_0	26.7	GPa
ρ_0	2.23	g cm^{-3}
c	4.65	$km\ s^{-1}$

S_1	0.22	None

2.1.4 Emission Spectrum and Temperature Model

We extract a temperature histogram from simulations at discrete times, using it to calculate an effective emission spectrum and effective temperature, T_{eff}, for comparison to pyrometry measurements. We first evaluate straightforward T^M mass-fraction weighted schemes for calculating T_{eff},

$$T_{eff} = \left[\sum_{i=0}^{N_{bins}} w_i T_i^M\right]^{1/M} \quad (6)$$

where N_{bins} is the number of emitter temperature bins, T_i is the different emitter temperatures, w_i is the mass fraction of each bin, and M is the temperature exponent. We set M = 1 for simple mass averaging and, separately, M = 4 which is akin to the Stefan-Boltzmann Law. We also evaluate Planck's Law which gives the spectral radiance, L , of a thermal body as,

$$L(T,\lambda)d\lambda = \epsilon(T,\lambda)\frac{2hc^2 d\lambda}{\lambda^5\left[e^{hc/k\lambda T}-1\right]} \quad (7)$$

where $\epsilon(T,\lambda)$ is the emissivity, λ is the wavelength, h is the Planck constant, k is the Boltzmann constant, and c is the speed of light. Similar to [19], we assume a gray body model, where the emissivity is independent of temperature and wavelength, and modify Planck's Law to account for multiple emitter temperature bins in a heterogeneous temperature field which simplifies to,

$$f(T_{eff}) = \left[e^{hc/k\lambda T_{eff}} - 1\right]^{-1} = \sum_{i=0}^{N_{bins}} \frac{w_i}{\left[e^{hc/k\lambda T_i} - 1\right]} \quad (8)$$

we solve for T_{eff} every 1 ns over the 30 ns duration of the simulation. Calculations are performed for wavelengths from 400 to 800 nm which is governed by the detectable emission spectrum of the pyrometer. In order to consistently converge, we set a minimum shocked mass threshold to 5% of the total HMX mass in the calculation. Also, in order to account for the shadowing effect of upstream shocked HMX by downstream unreacted particles, we fixed our sampling window for temperature calculations on a subset of HMX powder bed nearest the glass window.

3. Results and Discussion

Figure 1 shows the temperature and pressure fields in the shocked HMX powder bed simulations for a flyer impact speed of 1.4 km s^{-1} . At 10 ns, we observe shock compaction of the energetic grains, as well as initial HMX reaction and product gas formation. At 15 ns, the product gases permeate more of the powder bed and gas jetting occurs through focusing effects. At the same time, the shock continues transiting through the solid-gas mixture towards the glass window. At 20 ns, the shock reflects at the glass interface, which increases the pressure and temperatures in the HMX. Without the shock reflection, the peak HMX temperature would not be as pronounced and possibly more difficult to capture with a pyrometer.

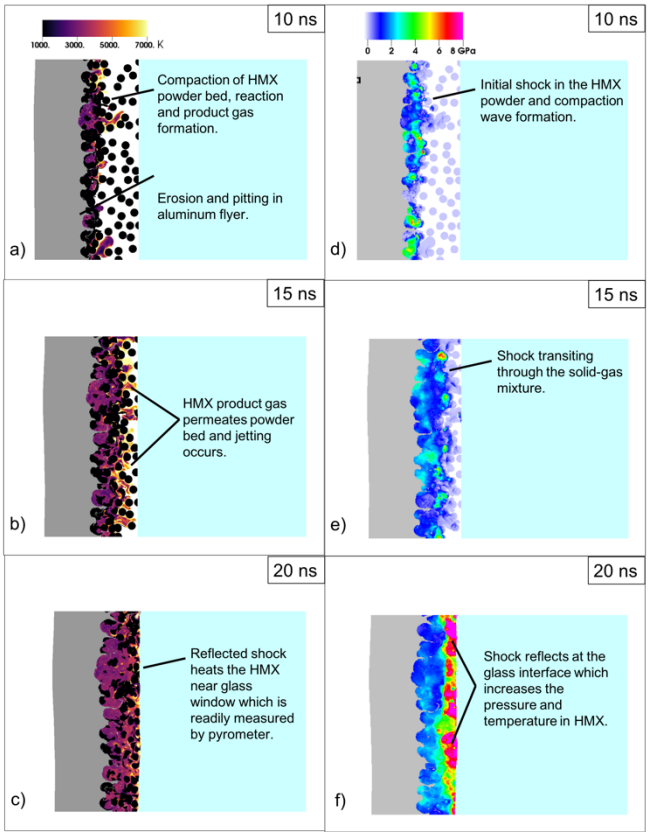

Figure 1. Calculated temperature (a-c) and pressure (d-e) fields in the shocked HMX powder bed for a flyer impact speed of 1.4 km s^{-1}. The HMX powder bed is 29% crystal density and the grain size is 4 μm.

Figure 2 shows the temperature and pressure fields in the shocked HMX powder bed simulations for a flyer impact speed of 3.6 km s^{-1}. Overall, the phenomena observed is qualitatively similar to the 1.4 km s^{-1} case but HMX pressures and temperatures are higher. At 5 ns, we observe the initial HMX shock compaction, reaction, product gas formation, as well as high speed product gas jetting evolving through focusing effects. More pronounced erosion and pitting is also observed in the aluminum flyer due to impact and reaction of HMX grains. At 7 ns, the product gases more fully permeate the powder bed and much more HMX is reacting than in lower impact velocity case. Shock reflection at the glass interface increases the pressure and temperatures in the HMX.

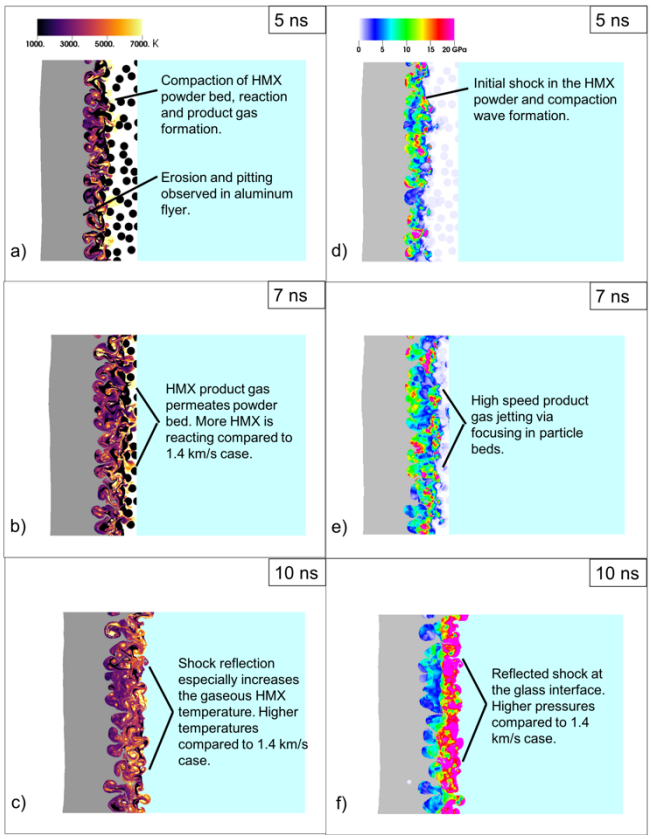

Figure 2. Calculated temperature (a-c) and pressure (d-e) fields in the shocked HMX powder bed for a flyer impact speed of 3.6 km s^{-1}. The HMX powder bed is 29% crystal density and the grain size is 4 μm.

Figure 3 shows the calculated T_{eff} of the shocked HMX sample for flyer impact speeds of 1.4, 2.8, and 3.6 km s^{-1} with pyrometry measurements [19, Fig 6]. Calculating T_{eff} using Planck's Law with a gray body assumption demonstrates good agreement with temperature data across all flyer impact speeds. T_{eff} is mostly within the experimental error bars across the 30 ns duration of the simulation. Peak T_{eff} for each impact case is well within the error bars. The peak temperatures for 1.4 and 2.8 km s^{-1} occur at 18 and 8 ns, respectively, which roughly corresponds to the initial reflected shock in HMX at the glass interface shown in Figures 1f and 2f. Peak T_{eff} values for the 2.8 and 3.6 km s^{-1} cases are comparable, suggesting that the hot spot mechanisms are similar despite different impact loading conditions. The T- and T^4-based averaging methods inadequately weight the higher temperature regions and result in a significantly lower T_{eff} that is in poor agreement with data. These methods give temperatures that are 2000-3000 K lower than peak values.

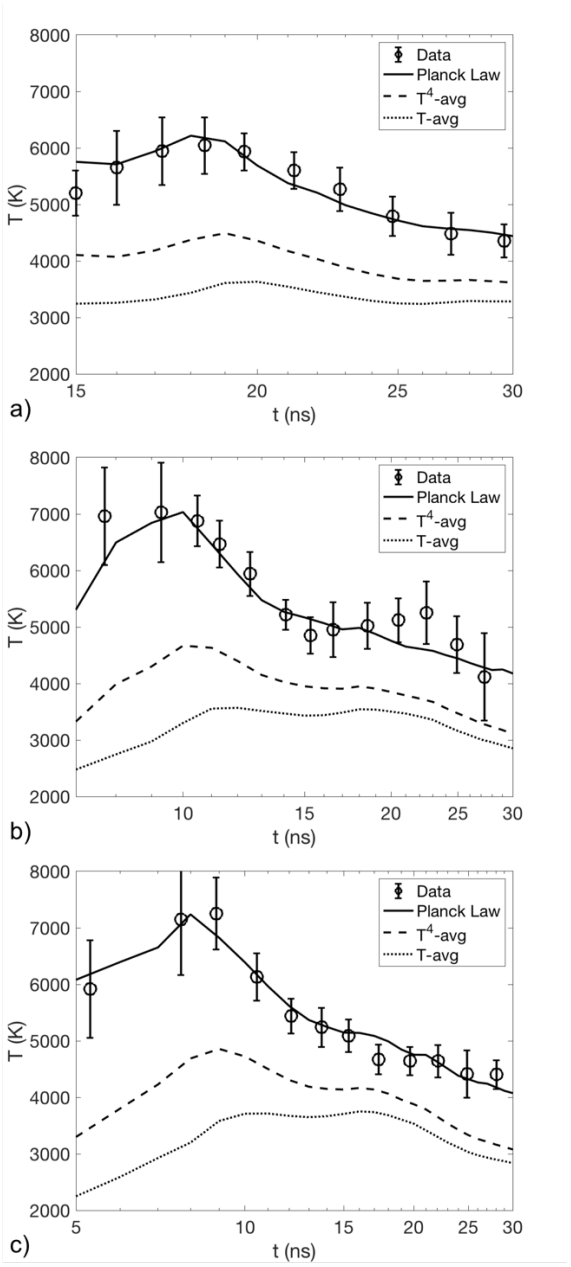

Figure 3. Calculated T_{eff} of the shocked HMX sample for flyer impact speeds of a) 1.4, b), 2.8, and c) 3.6 km s^{-1} compared to hot spot data [19, Fig 6]. Calculations using Planck's Law, T^4-based, and T-based methods are shown. The HMX powder bed is 29% crystal density and the grain size is 4 μm.

Figure 4 shows the HMX temperature distribution for a range of times near peak T_{eff} for flyer impact speeds of 2.8 and 3.6 km s^{-1}. For 2.8 km s^{-1}, we observe that the temperature distribution at 10 ns (time of peak T_{eff}) consists of approximately 1.5-3x more mass for T > 7500 K and less mass for T < 7500 K compared to the temperature distribution at 13 ns. While these hot spots only make up a small fraction of the overall mass, their greater weighting results in a >1000K difference in the calculated T_{eff} between 10 and 13 ns. Similar to the 2.8 km s^{-1} case, the temperature

distributions for the 3.6 km s^{-1} case has more mass for T > 7500 K and less mass for T < 7500 K at the 8 ns peak T_{eff} time compared to the 13 ns off-peak time. Similarities in the temperature distribution for the 2.8 and 3.6 km s^{-1} cases is the main cause for comparable T_{eff} peaks observed in Figure 3.

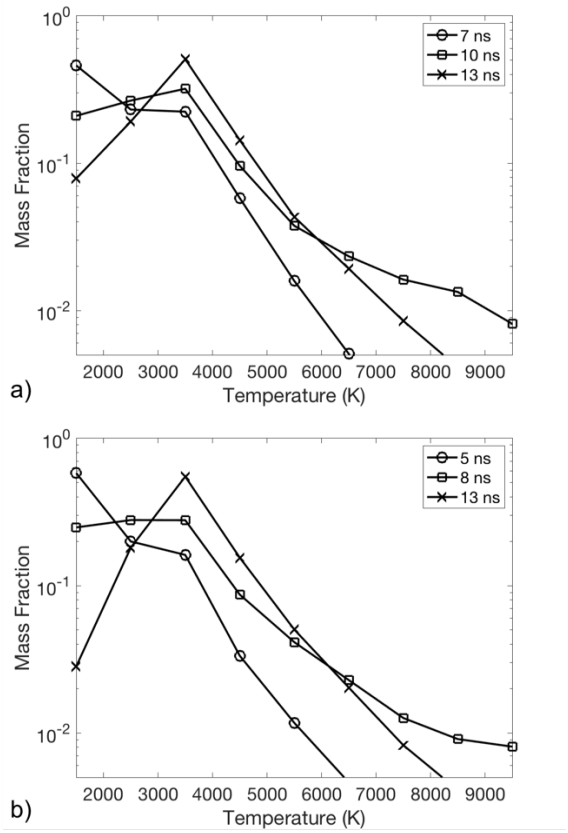

Figure 4. HMX temperature distribution for a range of times near peak T_{eff} for flyer impact speeds of a) 2.8 km s^{-1} and b) 3.6 km s^{-1}. The HMX powder bed is 29% crystal density and the grain size is 4 μm.

Figure 5 shows the HMX reaction rate ($^{dF}/_{dt}$) versus time for flyer impact speeds of 1.4, 2.8, and 3.6 km s^{-1}. The timing of peak $^{dF}/_{dt}$ (~8 ns, ~10 ns, and ~18 ns) are in good agreement with the timing of peak T_{eff} across flyer impact speeds in Figure 3. Peak $^{dF}/_{dt}$ increases with increasing impact speed. The shape of $^{dF}/_{dt}$ curves are similar for the two highest impact speeds but different than the lowest impact speed. For the 2.8 and 3.6 km s^{-1} cases, the induction time for reaction is 3-4 ns followed by a 5-6 ns period of acceleration to peak rate and then 7-9 ns deceleration. For the 1.4 km s^{-1} case, the induction time is 10 ns, the peak rate is 3x lower than the 2.8 km s^{-1}, and the post-peak rate doesn't decelerate substantially out to 30 ns; this suggests continued HMX grain burning late in time which is evident in Figure 1c.

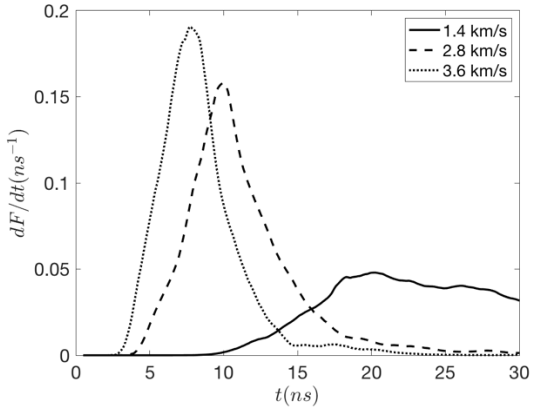

Figure 5. HMX reaction rate (*dF/dt*) versus time for flyer impact speeds of 1.4, 2.8, and 3.6 km s^{-1}.

Figure 6 shows the normalized reaction rate ($^{d\tilde{F}}/_{dt}$) versus the normalized extent of reaction ($\tilde{F}$) for flyer impact speeds of 1.4, 2.8, and 3.6 km s^{-1} where $^{d\tilde{F}}/_{dt} = {}^{1}/_{m_{grain}}{}^{dF}/_{dt}$, $\tilde{F} = {}^{m_{reacted}}/_{m_{grain}}$, and m_{grain} is the mass of a single 4 μm HMX grain. For increasing flyer impact speeds, we see that the peak $^{d\tilde{F}}/_{dt}$ ($^{d\tilde{F}_{peak}}/_{dt}$) increases and the location of the peak along $\tilde{F}$ also increases. We fit $^{d\tilde{F}}/_{dt}$ to a modified Arrhenius model that retains the original HMX activation energy (E_a) and prefactor (A_k),

$$d\tilde{\tilde{F}}/_{dt} = A_k e^{(-E_a R/T_{bulk} C_{mult})}(F_0 - \tilde{F})^a \tilde{F}^b F_0^{1-a-b} \qquad (9)$$

where T_{bulk} is the bulk shock temperature due to the aluminum flyer impact, C_{mult} is the multiplier on T_{bulk}, F_0 is the maximum value of $\tilde{F}$ (~70), and a,b are the form factor exponents for terms $F_0 - \tilde{F}$ and $\tilde{F}$. The additional term, F_0^{1-a-b}, is due to normalizing the Arrhenius form by m_{grain}. With E_a and A_k fixed, the fitting parameters are a, b, and C_{mult}. Fitting parameter values and bulk shock conditions for each impact speed are shown in Table 4.

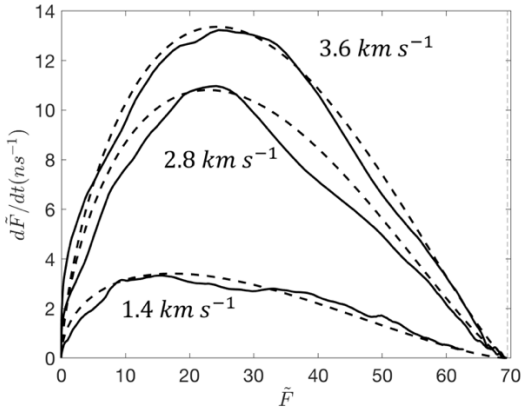

Figure 6. Normalized reaction rate ($^{d\tilde{F}}/_{dt}$) versus the normalized extent of reaction ($\tilde{F}$) for flyer impact speeds of 1.4, 2.8, and 3.6 km s^{-1}. Solid line is mesoscale simulation and dashed line is modified Arrhenius model.

Table 4. Rate Model Parameters (parameters unitless unless indicated).

Parameter	1.4 $km\ s^{-1}$	2.8 $km\ s^{-1}$	3.6 $km\ s^{-1}$
a	1.5	1.34	1.3
b	0.5	0.66	0.7
C_{mult}	3.30	2.07	1.64
T_{bulk}	468 K	840 K	1085 K
$C_{mult}T_{bulk}$	1544 K	1739 K	1779 K
P_{bulk}	5.5 GPa	19.8 GPa	28.1 GPa

In fitting these curves, we recognize that $a \neq b$ because ${}^{d\tilde{F}_{peak}}/_{dt}$ is not centered at $F_0/2$. Also, since the position of ${}^{d\tilde{F}_{peak}}/_{dt}$ shifts along $\tilde{F}$, the value of a, b changes with the flyer impact speed. This is due, in part, to the reaction mechanisms we observe in our simulations which does not follow idealized cylindrical burning described by $a, b = 0.5$ in previous studies [18]. To best match the acceleration and deceleration of rate curves, we set $a + b = 2$ across all flyer impact speeds. Setting the sum of exponents to a constant also ensures that the exponential term is primarily used to fit the amplitude rather than normalization term (F_0^{1-a-b}). T_{bulk} is determined according to the shock loading condition (see Table 4) and we vary C_{mult} to fit the peak rate value. C_{mult} increases with decreasing flyer impact speeds; this suggests that the lower shock loading cases more effectively heat the HMX than higher impact speed cases. This is consistent with previous literature where viscous heating due to pore collapse is more pronounced for lower pressure shocks especially below bulk melting [18]. Interestingly, the full temperature in the exponential term, $T_{bulk}C_{mult}$, for the 2.8 and 3.6 km s^{-1} cases are within a few percent of each other (1739 K and 1779 K) despite a >20% difference in T_{bulk} (840 K and 1085 K). In conjunction with earlier observations that the peak T_{eff} are also comparable, this suggests the reaction mechanisms may be converging at higher speeds and less dependent on the initial shock loading condition.

We also perform sensitivity studies to explore HMX powder bed density (increasing from 29% to 35% crystal density), grain size (doubling from 4 μm to 8 μm), HMX chemical kinetics (reducing Arrhenius prefactor), and spatial distribution of HMX grains to determine their influence on the predicted T_{eff}. These excursions are reasonable considering the uncertainties in powder HMX samples (density, grain size, spacing) and the uncertainties in the chemical kinetics which is based in part on the extrapolation of low pressure chemistry to the high pressure regime. Figure 7 shows the results of our sensitivity studies with comparisons to the baseline simulations and the pyrometry measurements; these comparisons help indicate whether a particular parameter sensitivity is meaningful.

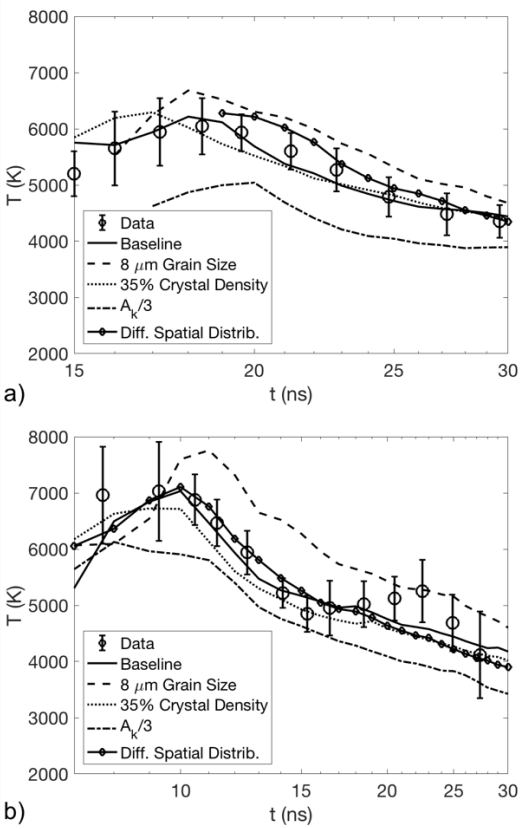

Figure 7. Calculated T_{eff} for sensitivity study on HMX powder bed density (increasing to 35% crystal density), grain size (increasing to 8 μm), HMX chemical kinetics (reducing Arrhenius prefactor by 1/3), and a different spatial distribution of HMX grains for impact speeds of a) 1.4 and b) 2.8 km s^{-1} compared to hot spot data [19, Fig 6]. Baseline simulations are also shown for reference.

For the larger 8 μm HMX grain size, we observe higher peak and post-peak T_{eff} than baseline at both impact speeds but it is more pronounced for the higher impact speed. This can be explained as follows: Pore sizes tend to scale with grain sizes and peak pore collapse temperatures scale with pore size; thus, higher temperatures can result from increasing the grain size. Since the spatial arrangement of energetic grains is not well defined, we simulate a different microstructural realization of the powder bed, fixing the grain size and volume fraction, to determine its influence on T_{eff}. A more pronounced effect is observed at the lower impact speed where T_{eff} is higher than the baseline value and nearly the value observed for the 8 μm grains. This suggests that the spatial arrangement is more important at lower impact speeds. This can be explained as follows: The lower degree of reaction leaves a random solid grain configuration through which the product gas permeates, jets, and impinges on the glass to stochastically form hot spots; thus, non-uniform microstructures can cause variations in T_{eff} because it is highly sensitive localized hot spots. We also reduce the Arrhenius prefactor to the baseline value in [24]; this tends to give us a lower T_{eff}. For a fixed shock loading and slower kinetics, less product gas can evolve. Reduced gas at the glass

interface means that there is less heating during shock reflection. The 35% crystal density HMX powder bed result is similar to the baseline density but there are two subtle differences. First, at an impact speed of 1.4 km s^{-1}, the peak T_{eff} are similar in magnitude but the 35% crystal density case arrives slightly earlier. This can result from higher density samples having a higher effective shock speeds and thus the shock reflection at the glass window occurs sooner. Second, there is a slightly lower temperature in the 35% crystal density case at 2.8 km s^{-1}. This can result from the reduced material jetting and gas formation for the lower porosity case. In the limit of zero porosity, there is no jetting and the peak temperature approaches the sample bulk shock temperature of the HMX.

4. Conclusions

- We validate reactive grain-scale simulations of low density HMX powder beds with hot spot temperature data over a range of shock loading conditions. These simulations are a useful tool for elucidating the role of hot spot mechanisms in the shock initiation of heterogeneous explosives. Validated grain-scale simulations also provide a basis for developing predictive morphology-aware models at the continuum scale, e.g., Statistical Hot Spot Model [32, 33].
- Calculating T_{eff} using Planck's Law with a gray body assumption demonstrates good agreement with hot spot temperature data over a range of shock loading conditions. In contrast, T^4- and T-based methods inadequately weight the higher temperature regions and result in a significantly lower T_{eff} that is in poor agreement with data. The method used to calculate an effective temperature is clearly a critical part of any hot spot analysis.
- A modified Arrhenius model is fit to the normalized reaction rates predicted by mesoscale simulations for our range of flyer impact speeds. Inferred temperatures ($T_{bulk}C_{mult}$) range from 1544 K to 1779 K which are quite similar considering the bulk shock temperature for the highest flyer speed is twice that of the lowest speed. Higher HMX heating efficiency suggests that a viscous mechanism is active at lower speed. This is consistent with previous literature where viscous heating due to pore collapse is more pronounced for lower pressure shocks especially below bulk melting [18].
- $T_{bulk}C_{mult}$ for the 2.8 and 3.6 km s^{-1} cases are within a few percent of each other despite a >20% difference in T_{bulk}. In conjunction with earlier observations that the peak T_{eff} are also comparable, this suggests the reaction mechanisms may be converging at higher speeds and less dependent on the initial shock loading condition.
- The present study shows greater sensitivities to reasonable excursions in HMX grain size, grain spacing, and chemical kinetics than to changes in powder bed density. Doubling the HMX grain size to 8 μm leads, for example, to higher T_{eff} while decreasing the Arrhenius prefactor by 1/3 yields significantly lower T_{eff}.
- We envision that future hot spot studies will consider validating reactive grain-scale simulations of high density plastic bonded explosives (PBXs). These are frequently used materials and such results would be of considerable practical value.

Acknowledgements

This work was performed under the auspices of the U.S. Department of Energy by Lawrence Livermore National Laboratory under Contract DE-AC52-07NA27344. The authors thank the Joint Munitions Program for partially funding this effort. LLNL-JRNL-774207-DRAFT.

Keywords: Hotspot • Mesoscale • Simulations • HMX • Modeling

References

[1] F. P. Bowden and A. D. Yoffe, Ignition and Growth of Explosions in Liquids and Solids (Cambridge University Press, 1952).
[2] A. W. Campbell, W. C. Davis, J. B. Ramsay, and J. R. Travis, Phys. Fluids 4 , 511–521 (1961).
[3] J. E. Field, G. M. Swallowe, and S. N. Heavens, Proc. Roy. Soc. Lond. A. Mat. 382 , 231–244 (1982).
[4] N. Bourne, Proc. R. Soc. A. 435 , p. 423 (1991).
[5] J. E. Field, Accounts Chem. Res. 25 , 489–496 (1992).
[6] B. Khasainov, B. Ermolaev, H.-N. Presles, and P. Vidal, Shock Waves 7 , 89–105 Apr (1997).
[7] D. J. Benson and P. Conley, Modell. Simul. Mater. Sci. Eng. 7 , 333–354 (1999).
[8] M. R. Baer, Thermochim. Acta 384 , 351–67 (2002).
[9] R. Menikoff and T. D. Sewell, Combust. Theor. Model. 6 , 103–125 (2002).
[10] J. E. Reaugh, "Grain-scale dynamics in explosives," Tech. Rep. UCRL-ID-150388-2002 (Lawrence Livermore National Laboratory, 2002).
[11] N. R. Barton, N. W. Winter, and J. E. Reaugh, Modell. Simul. Mater. Sci. Eng. 17 , p. 035003 (2009).
[12] A. Barua and M. Zhou, Modeling Simul. Mater. Sci. Eng. 19 , p. 055001 (2011).
[13] G. A. Levesque and P. Vitello, Propellants, Explosives, Pyrotechnics 40 , 303–308 (2014).
[14] R. A. Austin, N. R. Barton, J. E. Reaugh, and L. E. Fried, Journal of Applied Physics 117 , p. 185902 (2015).
[15] N. K. Rai and H. S. Udaykumar, Journal of Applied Physics 118 , p. 245905 (2015), https:// doi.org/ 10.1063/ 1.4938581 .
[16] R. A. Austin, H. K. Springer, and L. E. Fried, "Grain-scale simulation of shock initiation in composite high explosives," in Energetic Materials: From Cradle to Grave , edited by M. K. Shukla, V. M. Boddu, J. A. Steevens, R. Damavarapu, and J. Leszczynski (Springer International Publishing, Cham, 2017), pp. 243–270.
[17] N. K. Rai, M. J. Schmidt, and H. S. Udaykumar, Phys. Rev. Fluids 2 , p. 043202 (2017).
[18] H. Springer, S. Bastea, A. L. Nichols III, C. M. Tarver, and J. E. Reaugh, Propellants, Explosives, Pyrotechnics 43 , 805–817 (2018).
[19] W. P. Bassett and D. D. Dlott, Journal of Applied Physics 119 , p. 225103 (2016), https:// doi.org/ 10.1063/ 1.4953353 .

[20] W. P. Bassett and D. D. Dlott, Applied Physics Letters 109 , p. 091903 (2016), https:// doi.org/ 10.1063/ 1.4961619 .

[21] W. P. Bassett and D. D. Dlott, Review of Scientific Instruments 87 , p. 103107 (2016), https:// doi.org/ 10.1063/ 1.4964386 .

[22] C. R. Noble and et al, "ALE3D: An arbitrary Lagrangian-Eulerian multi-physics code," Tech. Rep. LLNLTR-732040 (LLNL, 2017).

[23] G. R. Johnson and W. H. Cook, Engineering Fracture Mechanics 21 , 31–48 (1985).

[24] B. F. Henson, B. W. Asay, L. B. Smilowitz, and P. M. Dickson, "Ignition chemistry in HMX from thermal explosion to detonation," Tech. Rep. LA-UR-01-3499 (Los Alamos National Laboratory, 2001).

[25] S. Bastea and L. E. Fried, "Chemical equilibrium detonation," in Shock Waves Science and Technology Library, Vol. 6: Detonation Dynamics , edited by F. Zhang (Springer Berlin Heidelberg, Berlin, Heidelberg, 2012), pp. 1–31.

[26] C.-S. Yoo and H. Cynn, The Journal of Chemical Physics 111 , 10229–10235 (1999).

[27] J. C. Gump and S. M. Peiris, Journal of Applied Physics 97 , p. 053513 (2005), https:// doi.org/ 10.1063/ 1.1856227 .

[28] S. P. Marsh, LASL Shock Hugoniot Data (University of California Press, Berkeley, CA, 1980).

[29] B. Olinger and et al, "The linear and volume compression of -hmx and rdx to 9 gpa," in Symp. (Int.) on High Dynamic Pressures (1979) p. 3.

[30] S. Bastea, "Chemical equilibrium and carbon kinetics in explosives," in Proceedings of the 15th International Detonation Symposium (2014) p. 896.

[31] S. Stekovic, H. K. Springer, M. Bhowmick, and D. D. Dlott, "Computational studies of laser-driven flyer impact experiments to probe properties of inert and energetic materials", in Proceedings of the 21st Biennial Conference of the APS Topical Group on Shock Compression of Condensed Matter, (2019) *Submitted*.

[32] A. L. Nichols and C. M. Tarver, 12th Int. Det. Symp. p. 489 (2003).

[33] A. L. Nichols, AIP Conf. Proc. 845 , p. 465 (2006).